Title
Experimental study on periodically forced interfacial gravity waves in a rotating cylindrical basin

Journal
International Symposium on Stratified Flows, 1(1)

Authors
Rojas, Pedro
Ulloa, Hugo
Niño, Yarko

Publication Date
2016-08-30

Experimental study on periodically forced interfacial gravity waves in a rotating cylindrical basin

By Pedro Rojas [1], Hugo Ulloa [1,2] & Yarko Niño [1,3]

Departamento de Ingenieria Civil, Universidad de Chile, pedrojas@ing.uchile.cl [1]
Mechanical and Aerospace Engineering, University of California, hulloasanchez@eng.ucsd.edu [2]
Advanced Mining Technology Center, Universidad de Chile, ynino@ing.uchile.cl [3]

Abstract

Diurnal wind-driven internal wave resonance regime, observed in stratified rotating lakes, was studied via laboratory experiments. The fundamental Kelvin wave (with a frequency ω_K) resonance dynamics was forced in a homogeneous water layer, inside a cylindrical basin mounted on a turntable, with a frequency $f/2$, via a periodic forcing mechanism, ω_w. The air-water interface displacement, η_ℓ, simulated the internal interface response of an immiscible two-layer stratified basin forced by Coriolis and a diurnal wind phase. This was achieved by controlling the ratio of the Rossby radius of deformation to the cylindrical radius, R_ℓ/R, the phase and the amplitude of a periodic forcing. Results showed strongly nonlinear wave dynamic regimes under idealized resonance conditions, $\omega_w/\omega_K \equiv 1$, on the shore, even for low energetic periodic forcings. Simultaneously, quasi-resonant states between other normal modes, such as Poincaré waves (with a frequency ω_P) and forcing sub-harmonics, $n\ \omega_w$, were identified in the offshore regions.

1 Introduction

The interaction between diurnal wind phase and the internal gravity wave field in stratified lakes can be understood as a forced harmonic oscillator system (Ockendon and Ockendon, 1973; Miles, 1984). Horizontal momentum flux forced by the wind shear is balanced by barotropic and baroclinic pressure gradients, disturbing thus the surface and internal interfaces of their equilibrium positions. During this process, a wide range of gravitational waves can be energized (Antenucci and Imberger, 2001). When the wind stops or becomes weaker in magnitude, the excited wave field propagates around the basin until damping mechanisms dissipate their energy (Shimizu and Imberger, 2009). However, the wind is typically periodic, so the interaction between wind and wave field can admit resonance regimes when the wind frequency (usually $\omega_w = 2\pi/T_d$, with $T_d = 24$ h) matches a fundamental frequency of the system (Antenucci and Imberger, 2003). Resonance interactions between wind forcing and large-scale gravitational waves have been identified in stratified lakes (Rozas et al., 2014). Observations have shown that diurnal gentle winds can significantly amplify the modal amplitude of waves located close to the resonant frequency (Rozas et al., 2014). Additionally, resonant regimes can drive nonlinear wave dynamics, such as wave steepening, non-hydrostatic dispersion or sub-harmonics, allowing energy transfer from resonant modes to other modes (Boegman and Ivey, 2012).

There are not many experimental studies on resonantly forced basin-scale waves in non-rotating basins (Thorpe, 1974; Miles, 1984; Wake et al., 2007; Boegman and Ivey, 2012), but less attention has had the wind/wave resonant regime in rotating basins (Rozas et al., 2014). Understanding resonant dynamic regimes and the quantification of the spatiotemporal distribution of the energy injected periodically by wind are key information to study transport processes in aquatic systems. The objective of this work is to study spatio-temporal dynamics of periodically forced gravity waves in rotating basins, as is the case of reservoirs or medium/large lakes located in extra/sub-tropical latitudes, respectively. These types of aquatic systems admit the existence of Kelvin and Poincaré waves (Csanady, 1967). In order to achieve this goal, laboratory experiments were conducted in a circular cylindrical acrylic tank mounted on a rotating turntable. Assuming that an n-layers stratified system can be expressed in n independent equations system

(Csanady, 1982; Stocker and Imberger, 2003), a one-layer system was adopted to emulate the dynamic of the internal interface in a two-layer stratified fluid. This simplification does not allow analyzing vertical mixing processes, but an adequate choice of rotation regime and the aspect ratio between vertical and horizontal scales of the water body can scale the dynamics of a stratified immiscible fluid. In this system, the waves spectrum is bounded by long gravity waves, that scale with the diameter of the cylinder, and capillary waves. However, this study focuses on the range of frequencies located between the fundamental Kelvin wave and nonlinear high-frequency solitary waves (see e.g., de la Fuente et al., 2008; Ulloa et al., 2014).

The article is structured as follows: i) control parameters are defined; ii) experimental setup and method are described; iii) results of time series (TS), power spectral density (PSD) and wavelet transform (WT) of the air-water interface displacement are presented; iv) finally, results are discussed in terms of background rotation, forcing frequency and space.

2 Theoretical formulation

Figure 1 shows an idealized cylindrical basin of radius R, with equivalent layer thickness h_ℓ (Csanady, 1982), density ρ_ℓ, inertial frequency f and vertical displacement of air-water interface η_ℓ. The system is periodically forced by an amplitude η_0 during a timescale $t_{W_{on}}$ and is relaxed during a timescale $t_{W_{off}}$, with a total time cycle of $T_{t_w} = t_{W_{on}} + t_{W_{off}}$. The gravity wave field dynamics has been controlled by two dimensionless parameters:

$$\mathcal{B} \equiv \frac{T_f}{T_g} = \frac{c_\ell T_f}{\lambda_h} \quad , \quad \mathcal{F} \equiv \frac{T_K}{T_w} = \frac{\omega_w}{\omega_K} \tag{1}$$

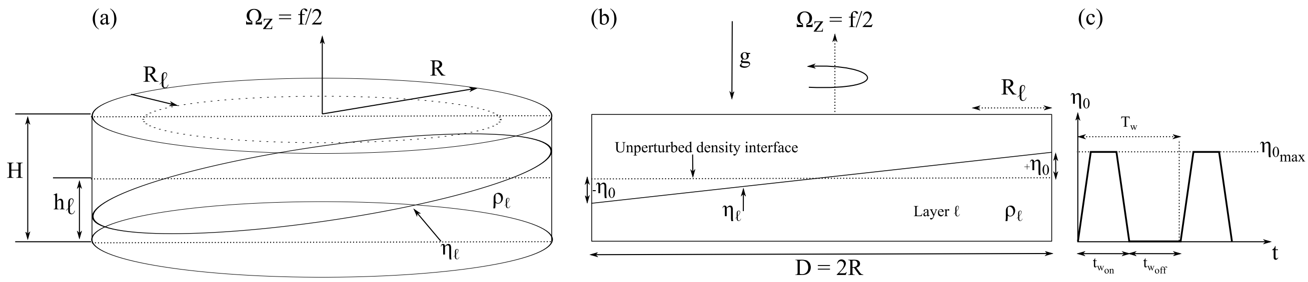

Figure 1: Conceptual model and controlled physical parameters.

The parameter $\mathcal{B}$ controls the effect of rotation on large-scale gravity waves. Here $\mathcal{T}_f = 2\pi/f$ corresponds to the local inertial period, while $\mathcal{T}_g = \lambda_h/c_\ell$ is the characteristic time-scale of gravity waves, where $\lambda_h = 2\pi R$ is a horizontal length-scale and $c_\ell = \sqrt{gh_\ell}$ is the linear speed of the wave, with g the acceleration of gravity (Figure 1 a, b). Hence, this parameter can be written as $\mathcal{B} = R_\ell/R$, where $R_\ell = c_\ell/f$ is the internal Rossby radius of deformation. The effect of rotation is more important in the dynamics of gravity waves as $\mathcal{B} \to 0$. Otherwise, the rotation effect is weak or neglected when $\mathcal{B} \to \infty$. We refer to this number as the rotation parameter or Burger number (Antenucci and Imberger, 2001).

The parameter $\mathcal{F}$ compares the timescale of the natural period of the system (in this case, the period of the fundamental Kelvin wave, T_K) with the timescale of idealized forcing wind, T_w (Figure 1 c). As $\mathcal{F} \to 1$, resonance regimes are expected in the system. In a regime of perfect resonance, $\mathcal{F} \equiv 1$, the energy is directly stored in the fundamental mode, inducing the increment of the modal amplitude until it is controlled by both linear mechanisms (gravity and viscosity) and nonlinear mechanisms (advection). Consequently, it is expected that the parameter $\mathcal{F}$ also affects the nonlinear dynamics of the gravity wave field.

Additionally, two other dimensionless parameters are used, which remain constant in all the experiments. The first is the amplitude parameter $\mathcal{A}_* \equiv \eta_{0_{max}}/h_\ell \equiv 0.15$, and it defines the maximun displacement of the forcing signal in terms of the ratio $\mathcal{A}_* \equiv \eta_{0_{max}}/h_\ell$(see Figure 1 c).

This parameter quantifies the work done by the wind to tilt the interface in a stationary regime. This value has been chosen to represent regular observed conditions in internal interfaces of two-layer stratified lakes (Antenucci and Imberger, 2003; Rozas et al., 2014). Although interface vertical displacements can be much larger under extreme wind conditions, this study focuses on exploring a 'normal' diurnal regime. The second parameter is associated with the wind phase structure and it is defined as $\mathcal{T}_w \equiv t_{W_{on}}/(t_{W_{on}} + t_{W_{off}}) \equiv 0.25$. This parameter describes a diurnal wind phase acting about 6 hours daily (e.g., Rozas et al., 2014).

It is important to note that linear normal modes (Kelvin and Poincaré waves) are obtained solving the eigenvalue problem derived from the inviscid linear equations, in an f-plane (Csanady, 1967; Stocker and Imberger, 2003).

3 Experimental Setup

Laboratory experiments were performed in a cylindrical tank (180 cm of diameter and 50 cm of depth) mounted on a turntable, whose angular velocity Ω_z varies from 0 to 6 r.p.m. Figure 2 shows a schematic of the experimental setup. An electro-hydraulic control allows tilting and releasing periodically an horizontal frame located between the cylindrical tank and the turntable, in short times ($t \approx 1$ s). The tank was filled with a water layer of thickness $h_\ell = 0.05$ m and density $\rho_\ell \approx 1000$ kg/m^3. Each experiment was conducted in two steps. First, the dimensionless parameters controlled in each experiment, $\mathcal{B}$ and $\mathcal{F}$ were set. The rotation parameter was achieved by spinning the turntable up until to get the inertial frequency $f = 2\ \Omega_z$ desired. The forcing parameter was achieved by setting the values for the initial amplitude $\mathcal{A}_*$ and the temporal distribution of wind $\mathcal{T}_w$. Second, the basin was periodically tilted and released to the horizontal position. This forcing induces a periodic adjustment of the air-water interface in response to both the horizontal barotropic gradient and rotation, exciting periodically the gravity wave field in the system.

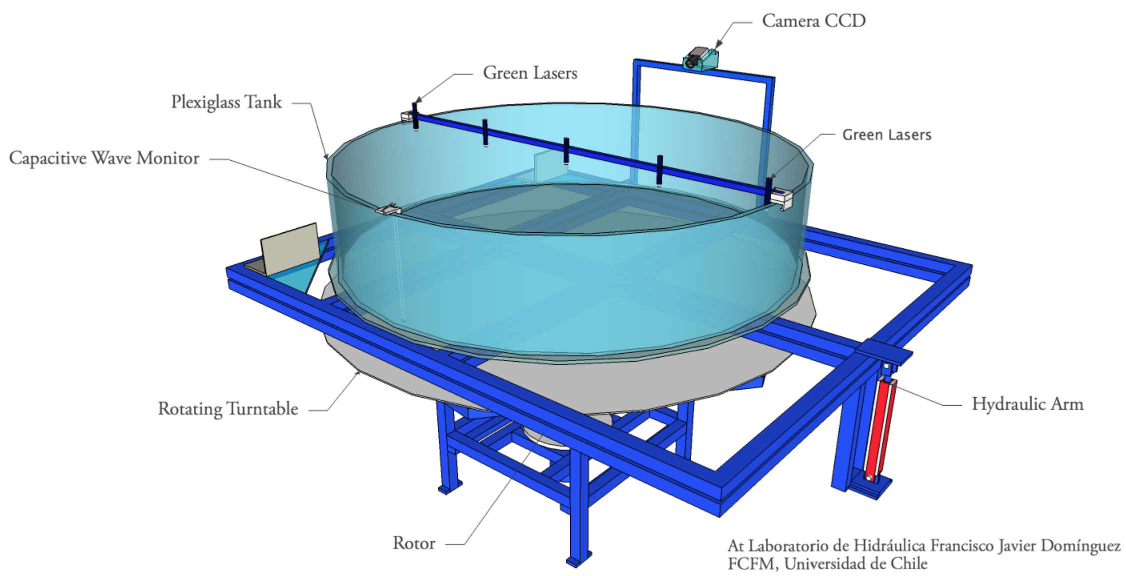

Figure 2: Schematic of the experimental setup.

The evolution of vertical displacement of the air-water interface was registered by combining an optical method of laser-induced fluorescence and a capacitive type sensor, which allow us to characterize the gravity wave field on both interior domain and boundary, respectively. For the first method a fluorescent sheet was created (along the diameter periodically tilted) using rhodamine to dye the water layer and a diametral green wavelength laser array (Figure 2). The fluorescent sheet was registered at 25 Hz using a CCD that rotates with the system. For the second method, a capacitive sensor (Churchill-Controls, model Wave Monitor) that sampled the water level at 100 Hz was used to capture the interface in the boundary, where $\eta_0(t = 0, r \approx 0.98\ R, \theta = -\pi/2) = 0$ (Figure 2). The set of experiments considered a total of 9 experiences, spanning 3 values for the rotation parameter, $\mathcal{B} = \{0.65, 1.00, 2.00\}$ and 3 values for the frequency of the periodic forcing, $\mathcal{F} = \{0.8, 1.0, 1.2\}$. The periodic disturbance, $\mathcal{A}_* = 0.15$ and temporal distribution of wind $\mathcal{T}_w = 0.25$ take constant values.

4 Results

Results of gravity wave field examined a sub-set of 6 experiments, considering 2 locations in the space (Figures 3, 4 for $r/R \approx 0.98$ and Figures 5, 6 for $r/R \approx 0.40$), 2 rotation extreme regimes $\mathcal{B} \in \{0.65, 2.00\}$ (moderate and weak rotation effect, respectively) and 3 forcing frequencies, $\mathcal{F} \in \{0.8, 1.0, 1.2\}$. Time series (TS) of the normalized interface displacement η_ℓ/h_ℓ and power spectral density (PSD) of the $\eta_\ell(t)/h_\ell$ are shown in Figures (3, 5), whereas wavelet transform (WT) of $\eta_\ell(t)/h_\ell$ are presented in Figures (4, 6).

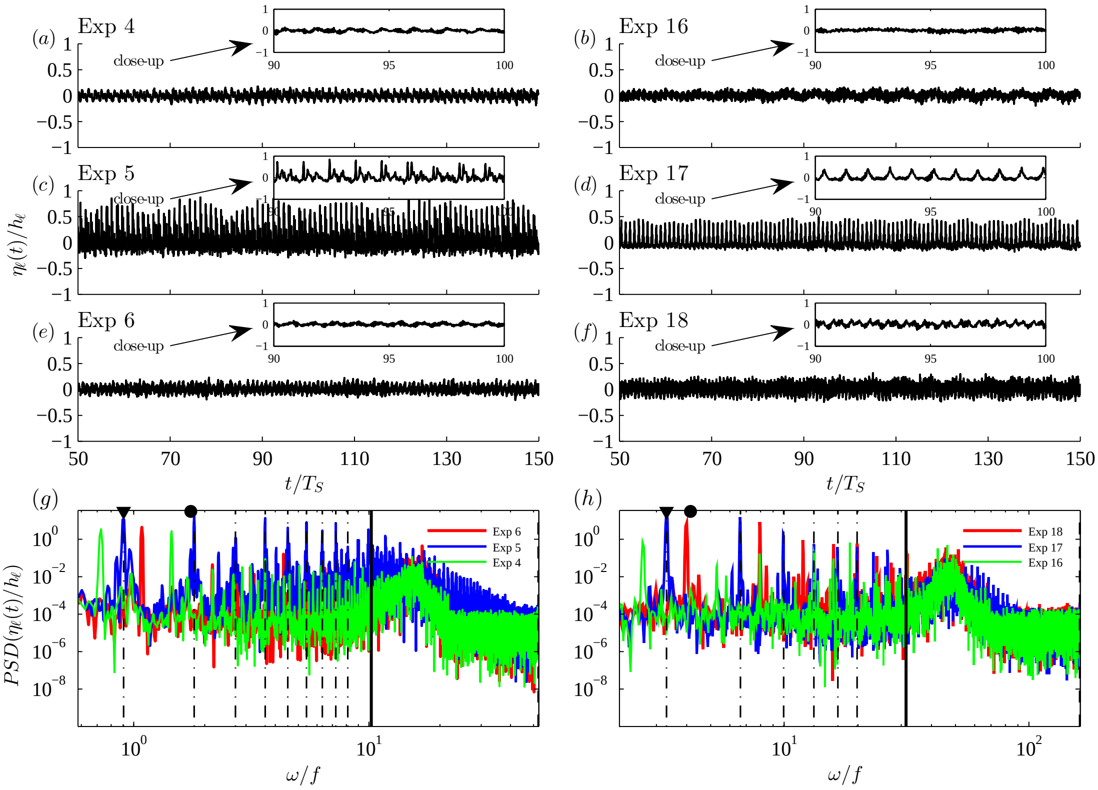

Figure 3: TS of interface displacement $\eta_\ell(t, r \approx 0.98\ R, \theta = -\pi/2) \pm \delta\eta_\ell$, with $\delta\eta_\ell \approx 2 \times 10^{-4}$m. Experiments considered are: $\mathcal{B} = 0.65 \pm 0.0014$ (a, c, e) and $\mathcal{B} = 2.00 \pm 0.0007$ (b, d, f). The forcing frequencies for the respective rows are $\mathcal{F} = 0.8 \pm 0.0016$ (a, b); $\mathcal{F} = 1 \pm 0.0016$ (c, d); $\mathcal{F} = 1.2 \pm 0.0016$; (e, f). Power spectral density (PSD): $\mathcal{F} = 0.8 \pm 0.0016$: green line; $\mathcal{F} = 1.0 \pm 0.0016$; blue line; $\mathcal{F} = 1.2 \pm 0.0016$; red line (g, h). Dot-dash line ($\cdot -$) correspond to the first 9 sub-harmonics of the forcing frequency $\mathcal{F} = 1.0 \pm 0.0016$. ▼: fundamental Kelvin wave frequency, ●: fundamental Poincaré wave frequency.

TS start at $t \approx 50\ T_S$, where $T_S = 4R/c_\ell$ is the period of the fundamental seiche. After $t \approx 50\ T_S$, the gravity wave field is found in a pseudo-steady state. In addition, the wave energy field in time/frequency space is calculated by wavelet transform technique (Torrence and Compo, 1998) for $90 < t/T_S < 100$. Energy is normalized by the maximum energy observed at the resonant forcing frequency ($\mathcal{F} = 1.0$).

Both TS and PSD exhibit significant differences depending on the rotation and the forcing frequency at $r/R \approx 0.98$. Higher amplitudes of η_ℓ/h_ℓ are observed in experiments in which

$\mathcal{F} = 1.0$ (Figure 3 c, d), in agreement with Rozas et al. (2014). In this resonant regime, basin-scale waves show a strongly nonlinear degeneration along with the formation of solitary type waves when $\mathcal{B} = 0.65$ (moderate rotation). The nonlinear dynamic enhances the transfer of energy from large to smaller scales (see close-up Figure 3 c). Energy peaks are observed at harmonic frequencies of the primary forced mode (see dash-dot lines in Figures 3 g, h) for both rotation regimes when $\mathcal{F} = 1.0$ (blue lines of Figures 3 g, h). In addition, the PSD of moderate rotation shows a wider energized normalized frequency bandwidth and higher energy peaks at harmonics frequencies than the PSD of weak rotation (compare figures 3 g and 3 h).

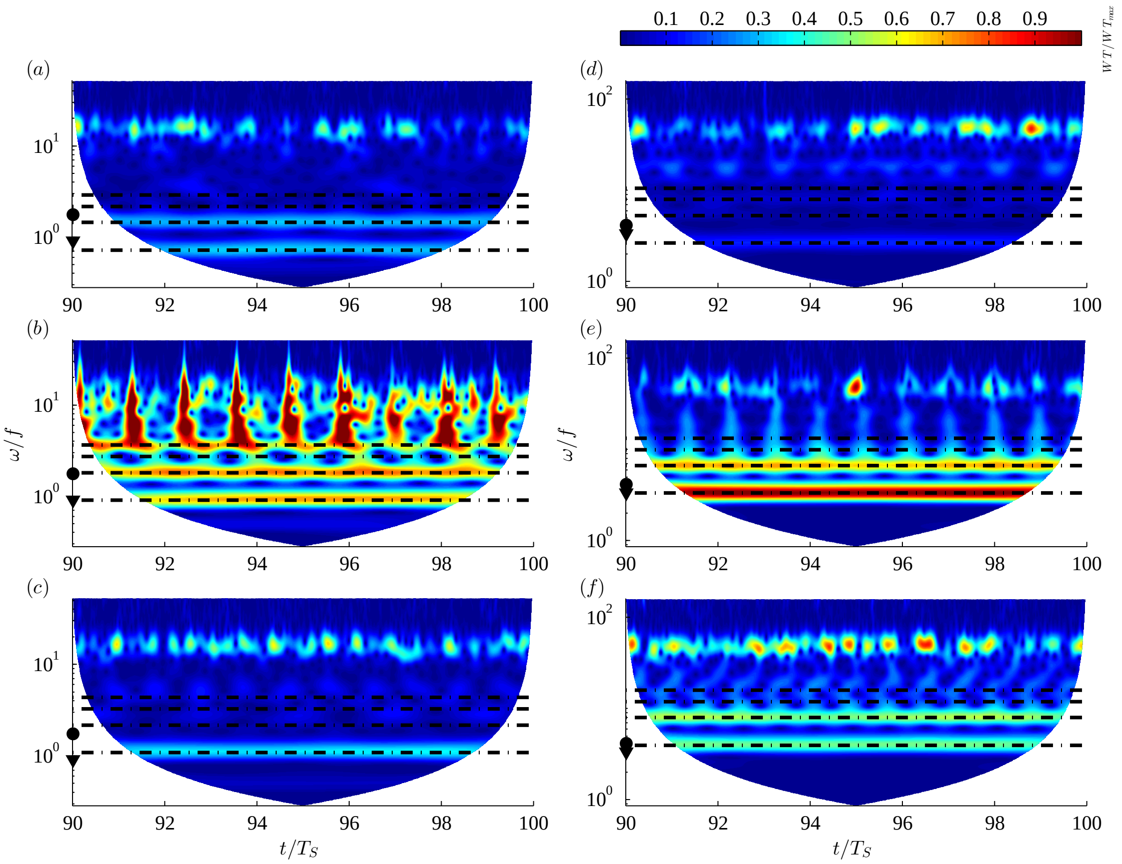

Figure 4: WT of the vertical displacement of the interface $\eta_\ell(t, r \approx 0.98\ R, \theta = -\pi/2) \pm \delta\eta_\ell$ with $\delta\eta_\ell \approx 2 \times 10^{-4}$m. Experiments considered are: $\mathcal{B} = 0.65 \pm 0.0014$ (a, b, c) and $\mathcal{B} = 2.00 \pm 0.0007$ (d, e, f). The forcing frequencies for the respective rows are: $\mathcal{F} = 0.8 \pm 0.0016$ (a, d); $\mathcal{F} = 1 \pm 0.0016$ (b, e); $\mathcal{F} = 1.2 \pm 0.0016$; (c, f). Dot-dash lines ($\cdot -$) represent the first 4 sub-harmonic modes for each $\mathcal{F}$ condition (from the bottom upwards.)

High-frequency bandwidth is energized periodically ($4 < \omega/f < 11$) due to energy transfer driven by nonlinear processes, as $\mathcal{F} \to 1$ and for a moderate rotation regime (Figure 4 b). Furthermore, first and second harmonic modes (first and second horizontal dot-dash lines $\cdot -$) are periodically energized. Otherwise, absence of nonlinear processes lead to energy remains at first harmonic, as $\mathcal{F} \to 1$ and $\mathcal{B} \approx 2$ (Figure 4 e). Moreover, sub-resonant and super-resonant experiments (i.e $\mathcal{F} = 0.8$ and $\mathcal{F} = 1.2$, respectively) show a different behavior only when the effect of rotation is weak. Here, low and high frequencies have higher energy peaks with $\mathcal{F} = 1.2$ (Figure 4 f).

Both TS and PSD exhibit clear differences in terms of rotating regime and the forcing frequency at $r/R \approx 0.40$. Larger wave amplitudes are observed for weak rotating regime when $\mathcal{F} = 0.8$ and $\mathcal{F} = 1.2$ (Figures 5 b, f) and for moderate rotating regime when $\mathcal{F} = 1.0$ (Figure 5 c). This can be understood in terms of the energy distribution as function of the Rossby radius of deformation (R_ℓ). Weaker rotating regimes can store more potential energy than moderate ro-

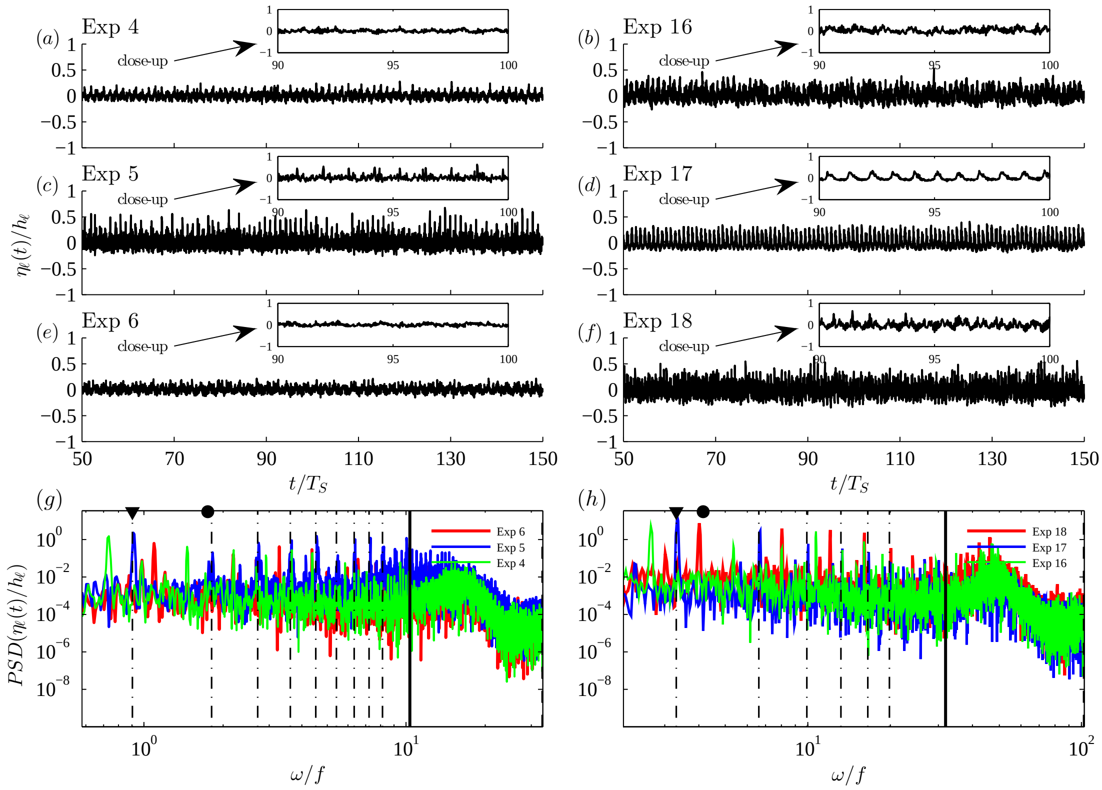

Figure 5: TS of interface displacement $\eta_\ell(t, r \approx 0.40\ R, \theta = 0) \pm \delta\eta_\ell$, with $\delta\eta_\ell \approx 2 \times 10^{-4}$m. Idem Figure 3.

tating regimes within the Rossby radius of deformation (Antenucci and Imberger, 2001; Stocker and Imberger, 2003), regardless the forcing frequency. Then, weaker rotations allow higher amplitudes in the interior. However, under stronger rotating regimes, the combination of nonlinear wave dynamics and resonance forcing frequency (Figure 5 c) can lead to higher wave amplitudes. Furthermore, regardless the rotating regime, nonlinear steepening processes are not longer evident in the interior domain. Energy peaks are observed at harmonics of the primary forced mode (see dash-dot linen in Figures 5 g, h) for both rotation regimes with $\mathcal{F} = 1.0$ (blue lines of Figures 5 g, h). As is observed on the boundary ($r/R \approx 0.98$), peaks show a different behavior as a function of Burger number. For the weak rotation, high-frequency harmonic bandwidth is narrower than the moderate rotation. In addition, the higher energy peak for both rotations is located at the first harmonic (resonance state between the forcing and the fundamental Kelvin wave $\blacktriangledown$).

For a moderate rotation regime (Figure 6 b), the interior region ($r/R \approx 0.40$) shows that the high-frequency bandwidth ($6 < \omega/f < 11$) is intermittently energized, following a complex time pattern. This result suggests the existence of other nonlinear degeneration mechanisms in the interior basin (Grimshaw et al., 2013), which are not necessary associated with nonlinear processes driven by wave steepening. Moreover, both rotation regimes show that the first harmonic is continuously energized in terms of time (see Figure 6), being more intense when rotation is weak (first horizontal dot-dash lines $\cdot -$ in Figure 6 d, e, f). Otherwise, sub-resonant and super-resonant experiments (i.e., $\mathcal{F} = 0.8$ and $\mathcal{F} = 1.2$, respectively) exhibit a different behaviour only when the effect of rotation is weak. Here, low and high frequencies have higher energy with $\mathcal{F} = 1.2$ (Figure 4 f). Finally, high-frequency energy is higher with respect to energy observed at $r/R \approx 0.98$ (Figure 6 d,f).

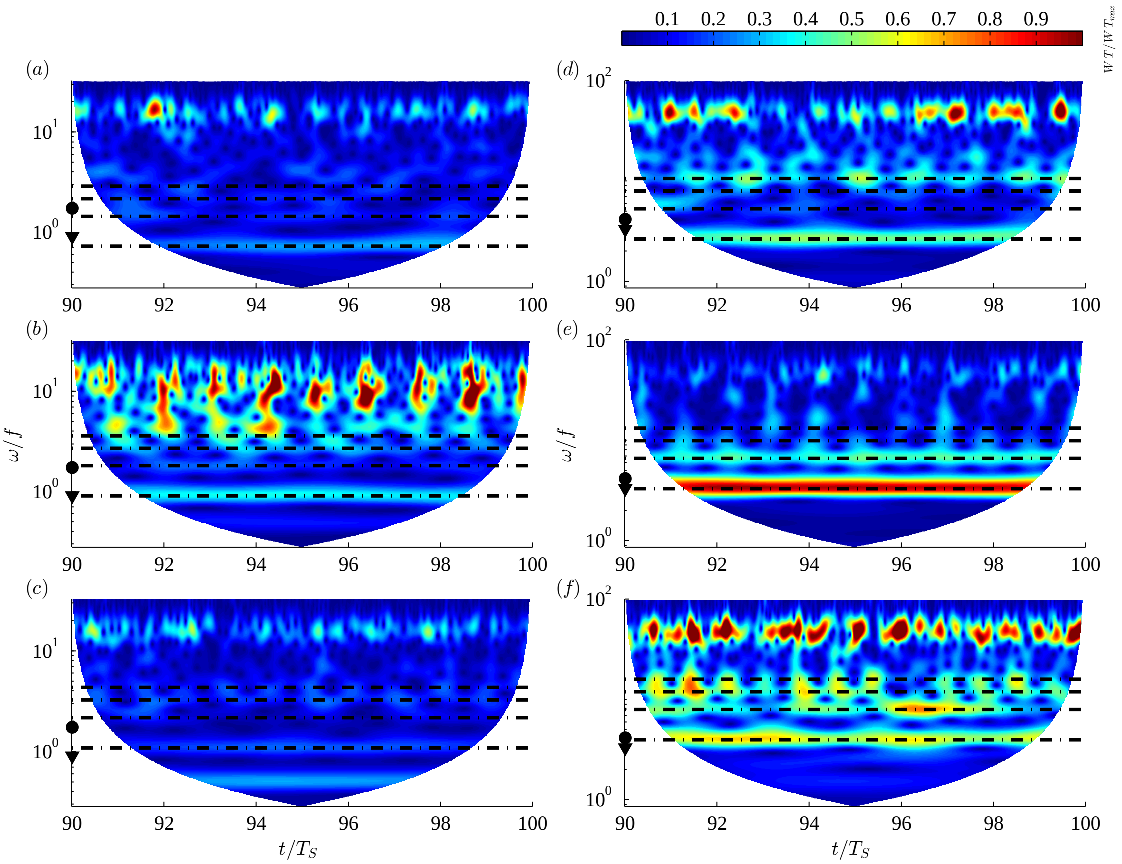

Figure 6: WT of the vertical displacements of the interface $\eta_\ell(t, r \approx 0.40\ R, \theta = 0) \pm \delta\eta_\ell$, with $\delta\eta_\ell \approx 2 \times 10^{-4}$m. Idem Figure 4.

5 Discussion

In this work, laboratory experiments were conducted to study the spatiotemporal response of a periodically forced fluid in an ambient where the rotation effect is not negligible, motivated by field observations that showed resonance regime between the diurnal wind forcing and large-scale gravitational waves (Antenucci and Imberger, 2003; Rozas et al., 2014). The results exhibit similar resonance regime between the fundamental Kelvin mode (▼) and the primary forced mode (or first harmonic, with $\mathcal{F} = 1$) observed previously by Rozas et al. (2014) in a rectangular domain. The role of rotation in the nonlinear dynamic of boundary trapped large-scale waves is robust and it has been studied in previous works (Sakai and Redekopp, 2010; Ulloa et al., 2014). In this work we show that a quasi-steady nonlinear/non-hydrostatic wave regime is achieved when the rotating flow is periodically forced at the resonance frequency, $\mathcal{F} = 1$, even for low forcing magnitudes. Furthermore, there is a quasi-resonance state between the fundamental Poincaré (●) wave and the first harmonic of the wind forcing, for $\mathcal{F} = 1.2$ and weak rotation. This result could explain the degeneration and spectral energy distribution at high-frequencies in the interior basin (see Figure 6 f), as a consequence of other energy transfer mechanisms associated to Poincaré waves, which could be independent of those nonlinear mechanisms that drive the Kelvin wave degeneration. Furthermore, this pseudo-resonant state demonstrates the higher energy contained at low frequencies as $\mathcal{F} = 1.2$ with respect to $\mathcal{F} = 0.8$. The Poincaré wave has a second pseudo-resonant regime with the second harmonic of $\mathcal{F} = 1$ when $\mathcal{B} = 0.65$. As $r/R \to 0$, the energy contained in this resonant regime is lower (see Figures 3; 5g) due to the radial energy decay as a function of the Rossby radius of deformation. Further research is required to quantify the effect of viscous dissipation in the resonance regime.

References

Antenucci, J. and Imberger, J. (2001). Energetics of long internal gravity waves in large lakes. *Limnol. Oceanogr.*, 46:1760–1773, doi:10.4319/lo.2001.46.7.1760.

Antenucci, J. P. and Imberger, J. (2003). The seasonal evolution of wind/internal wave resonance in lake kinneret. *Limnol. Oceanogr.*, 48(5):2055–2061, doi:10.4319/lo.2003.48.5.2055.

Boegman, L. and Ivey, G. N. (2012). The dynamics of internal wave resonance in periodically forced narrow basins. *J. Geophys. Res*, 117(C11):doi:10.1029/2012JC008134.

Csanady, G. T. (1967). Large-scale motion in the great lakes. *J. Geophys. Res.*, 72:4151–4162, doi:10.1029/JZ072i016p04151.

Csanady, G. T. (1982). On the Structure of Transient Upwelling Events. *J. Phys. Onceanogr.*, 12:84–96, dx.doi.org/10.1175/1520--0485(1982)012<0084:OTSOTU>2.0.CO;2.

de la Fuente, A., Shimizu, K., Imberger, J., and Niño, Y. (2008). The evolution of internal waves in a rotating, stratified, circular basin and the influence of weakly nonlinear and nonhydrostatic accelerations. *Limnol. Oceanogr.*, 53(6):2738–2748, dx.doi.org/10.4319/lo.2008.53.6.2738.

Grimshaw, R. H. J., Helfrich, K. R., and Johnson, E. R. (2013). Experimental study of the effect of rotation on large amplitude internal waves. *Phys. Fluids*, 25:056602, doi:10.1063/1.4805092.

Miles, J. W. (1984). Resonantly forced surface waves in a circular cylinder. *J. Fluid Mech.*, 149:15–31, doi:10.1017/S0022112084002512.

Ockendon, J. and Ockendon, H. (1973). Resonant surface waves. *J. Fluid Mech.*, 59(02):397–413, doi:10.1017/S0022112073001618.

Rozas, C., de la Fuente, A., Ulloa, H., Davies, P., and Niño, Y. (2014). Quantifying the effect of wind on internal wave resonance in lake Villarrica, Chile. *Environ. Fluid Mech.*, 14 (4):849–871, doi:10.1007/s10652--013--9329--9.

Sakai, T. and Redekopp, L. G. (2010). A weakly nonlinear evolution model for long internal waves in a large lake. *J. Fluid Mech.*, 637:137–172, dx.doi.org/10.1017/S0022112010001114.

Shimizu, K. and Imberger, J. (2009). Damping mechanisms of internal waves in constinuously stratified rotating basins. *J. Fluid Mech.*, 637:137–172, doi:10.1017/S0022112009008039.

Stocker, R. and Imberger, J. (2003). Energy Partitioning and Horizontal Dispersion in a Stratified Rotating Lake. *J. Phys. Oceanogr.*, 33:512–529, dx.doi.org/10.1175/1520--0485(2003)033<0512:EPAHDI>2.0.CO;2.

Thorpe, S. (1974). Near-resonant forcing in a shallow two-layer fluid: a model for the internal surge in loch new? *J. Fluid Mech.*, 63(03):509–527, doi:10.1017/S0022112074001753.

Torrence, C. and Compo, G. P. (1998). A practical guide to wavelet analysis. *Bulletin of the American Meteorological society*, 79(1):61–78, dx.doi.org\/10.1175\/1520--0477(1998)079<0061:apgtwa>2.0.co.

Ulloa, H. N., de la Fuente, A., and Niño, Y. (2014). An experimental study of the free evolution of rotating, nonlinear internal gravity waves in a two-layer stratified fluid. *J. Fluid Mech.*, 742:308–339, dx.doi.org/10.1017/jfm.2014.10.

Wake, G. W., Hopfinger, E. J., and Ivey, G. N. (2007). Experimental study on resonantly forced interfacial waves in a stratified circular cylindrical basin. *J. Fluid Mech*, 582:203–222, doi:10.1017/S002211200700585X.